Ceramics International 42 (2016) 9058–9064

Contents lists available at ScienceDirect

Ceramics International

journal homepage: www.elsevier.com/locate/ceramint

Influence of microwave-assisted hydrothermal treatment on the properties of nickel oxide–zirconia based composites

L.B. Pinheiro [a], F.N. Tabuti [a], A.E. Martinelli [b], F.C. Fonseca [a,*]

[a] Instituto de Pesquisas Energéticas e Nucleares, IPEN-CNEN/SP, São Paulo, SP 05508-000, Brazil
[b] Universidade Federal do Rio Grande do Norte, UFRN, Natal, RN 59072-970, Brazil

ARTICLE INFO

Article history:
Received 15 January 2016
Received in revised form
20 February 2016
Accepted 27 February 2016
Available online 28 February 2016

Keywords:
Ceramic composites
Coprecipitation
Microwave-assisted hydrothermal
Impedance spectroscopy

ABSTRACT

The influence of a microwave-assisted hydrothermal treatment (MWH) on the properties of NiO–ZrO_2:8 mol%Y_2O_3–CeO_2 composite was investigated. The composites were prepared by coprecipitation of nickel and cerium salts in a suspension of ZrO_2:8 mol%Y_2O_3 (YSZ). Simultaneous thermogravimetric and differential thermal analysis revealed that the MWH promotes the crystallization of $Ni(OH)_2$, as confirmed by X-ray diffraction. The sintering behavior of ceramic compacts was influenced by the MWH treatment, which contributed to slightly higher final apparent densities. Impedance spectroscopy measurements revealed that the electrical properties of sintered composites exhibit characteristics of mixed-ionic–electronic conductors, a feature that was suppressed in the samples that underwent MHW treatment. Such an effect evidences the influence of hydrothermal treatment on the final microstructure of the composite.

1. Introduction

Ceramic-supported Ni composites are studied for different applications in catalysis and electrochemistry. For example, Ni-ZrO_2:8 mol%Y_2O_3 (Ni–YSZ) cermet is the standard anode material of solid oxide fuel cells (SOFC) having excellent properties, unheard by any other alternative material proposed for H_2 fuelled applications. Limitations due to low redox stability and sintering of Ni particles at high operating temperatures are compensated by both the high electronic conductivity and electrocatalytic activity [1]. One of the main strategies for enhancing the properties of fuel cell anode (or other catalytic systems [2]) is to tailor the microstructure by a strict control of the synthesis method. By controlling parameters such as particle size and distribution of both the ceramic and metallic phases can result in enhanced properties of the cermet [3,4]. The nickel content strongly influences the electrical conductivity of the cermet, which usually requires relative volume fractions above the percolation threshold (~30 vol%). The electrical conductivity is also dependent on the microstructure and small particle size of Ni with high dispersion in the YSZ skeleton usually results in lower percolation threshold and better redox resistance [3–6]. Thus, a wide range of synthesis techniques has been reported for this cermet, such as, liquid mixture [6], gel-precipitation [7] and combustion method [8].

Aiming at applications requiring high-performance cermets chemical synthesis routes are preferable over traditional solid-state reaction to attain the desired Ni particle size. Particularly the coprecipitation technique is efficient to synthesize particles with reduced size and homogeneous size distribution [9]. Such technique has been used for the synthesis of NiO–YSZ composites [10–12]. Nevertheless, the main problem is to avoid the formation of Ni complexes during the coprecipitation. However, by controlling the pH it is possible to obtain highly dispersed and homogeneous powders [11].

It is known that microwave energy can improve reaction kinetics, selectivity and yield of chemical reactions [13]. Therefore, synthesis techniques based on chemical routes assisted by microwave treatments can benefit from such characteristics. Combustion [14–16] and hydrothermal synthesis [17–19] are some techniques usually modified for microwave-assisted heating. In general, such studies showed a narrow particle size distribution and better homogeneity in the final product in comparison with the corresponding conventional synthesis methods. These improved properties are attributed to unique thermal effects in microwave-heated materials, such as volumetric heating and inverse temperature gradient [20].

In the present study, NiO–YSZ was synthesized with small addition of CeO_2. The addition of ceria aims at enhancing catalytic activity of the composite [21,22]. Powders were synthesized by hydroxide coprecipitation method followed by a microwave-assisted hydrothermal (MWH) treatment aiming at the preparation of homogeneous composites. The influence of the MWH treatment

* Corresponding author.
E-mail address: fabiocf@usp.br (F.C. Fonseca).

http://dx.doi.org/10.1016/j.ceramint.2016.02.165
0272-8842/

was investigated and results compared with conventional heat-treatment.

2. Experimental

2.1. Synthesis of NiO–YSZ–CeO_2 powders

NiO–YSZ–CeO_2 powders with nominal composition NiO:YSZ:CeO_2=56:34:10 (wt%) were prepared by hydroxide coprecipitation method. Such nominal composition was chosen to result in samples with final NiO content close to the theoretical percolation threshold of NiO (~30 vol%) in order to enhance possible effects due to the different thermal treatments studied. Nevertheless, the final composition is within the range used for the NiO–YSZ SOFC composite anodes and other possible applications such as catalysts for chemical vapor deposition of carbon nanotubes [23]. The starting materials were $Ni(CH_3COO)_2 \cdot 4H_2O$ (Aldrich), $Ce(NO_3)_3 \cdot 6H_2O$ (Aldrich), ZrO_2:8 mol%Y_2O_3 (Tosoh), and NH_4OH (Vetec) as precipitation agent. The appropriate amounts of $Ni(CH_3COO)_2 \cdot 4H_2O$ and $Ce(NO_3)_3 \cdot 6H_2O$ were dissolved in distilled water (Ni^{2+} ion concentration: 0.1 mol L^{-1}) under continuous magnetic stirring to obtain a homogeneous solution. The YSZ powder was added to the solution and the resulting suspension was heated at 95 °C. The NH_4OH:H_2O (1:1 volume) was added dropwise to the suspension until pH=9.5 was reached, thereby forming the precipitate.

The precipitate mixed with YSZ powder was filtered and washed with distilled water and ethanol several times for complete removal of ions NH^{4+}, NO_4^-, and CH_3COO^{2-}. After washing, precipitates were dried at 100 °C for 12 h. The as-prepared powder was heat treated by two different methods: i) microwave-assisted hydrothermal (MWH) and ii) conventional heat treatment (CH). The microwave-assisted hydrothermal treatment was performed by placing the material in water suspension into teflon containers. The sealed Teflon containers were inserted into an autoclave and heated in microwave oven (800 W, 2.45 GHz) at 130 °C for 2 h with 10 °C min^{-1} heating rate. The average pressure achieved in this heating condition was 1.4 atm. The conventional heat treatment (CH) of powders was carried in an oven pre-heated at 130 °C for 2 h. The as-prepared powder along with both MWH and CH materials were calcined in air at 500 °C for 4 h to obtain NiO–YSZ–CeO_2 powders.

2.2. Characterization of NiO–YSZ–CeO_2

The thermal decomposition of the as-prepared, MHW, CH, and calcined powders were studied by simultaneous thermogravimetry (TG) and differential thermal analysis (DTA) using a Seteram Labsys. The maximum temperature was 1200 °C with 10 °C min^{-1} heating rate in synthetic air flow (50 mL min^{-1}). The chemical compositions of the calcined samples were determined through energy dispersive X-ray spectroscopy (EDX). The linear shrinkage of pellets (7 mm diameter) uniaxially pressed (4 MPa) was measured using a Setaram Labsys dilatometer up to 1400 °C with 10 °C min^{-1} heating rate in air flow (50 mL min^{-1}). X-ray powder diffraction (XRD) analyses were carried out for phase identification in a Rigaku-Miniflex II operating at 30 kV, 15 mA, 0.05° 2θ° step and 2 s counting time, using $Cu_{k\alpha 1}$ radiation (λ=1.5406 Å). The crystallite sizes were calculated using Scherrer formula [24,25].

The electrical properties of pellets sintered at 1200 °C for 3 h were studied by impedance spectroscopy (IS) using a Solartron 1260 frequency analyzer in the 1 Hz–30 MHz frequency range with 200 mV ac amplitude (zero bias dc). Such an amplitude was found to be within the ohmic range for such measurements. The IS measurements were carried out in static ambient air in the 100–700 °C temperature range, allowing the system stabilize at each measuring temperature for at least 30 min. For IS measurements, silver contacts were deposited onto the parallel surfaces of the samples (typically, ~8 mm diameter and 1 mm thickness) and cured at 600 °C for 1 h [26].

The morphology of fractured surfaces of sintered samples was investigated by field emission gun scanning electron microscopy (FEG-SEM) using a FEI Inspect F50 microscope operating at 5 kV.

3. Results and discussion

Thermogravimetric (TG) and differential thermal analysis (DTA) curves for the as-prepared, CH, and MWH powders are shown in Fig. 1. The as-prepared and CH samples exhibited three main mass loss events up to 1200 °C taking place at similar temperatures T~100, 280, and 390 °C. The MWH sample showed two mass loss events at T~100 and 305 °C.

The initial mass loss at T~100 °C is attributed to water desorbed from the surface of the powders and corresponds to ~6%, 5%, and 3% for the as-prepared, CH, and MWH samples, respectively. The total mass loss depends on the thermal history of the powders and it was found to be 24%, 20%, and 15% for the as-prepared, CH, and MWH samples, respectively. Nevertheless, the main differences observed in thermal decomposition of the samples arise when the TG/DTA curves are analyzed in the temperature range of the main mass loss events (Fig. 1b). The mass loss is

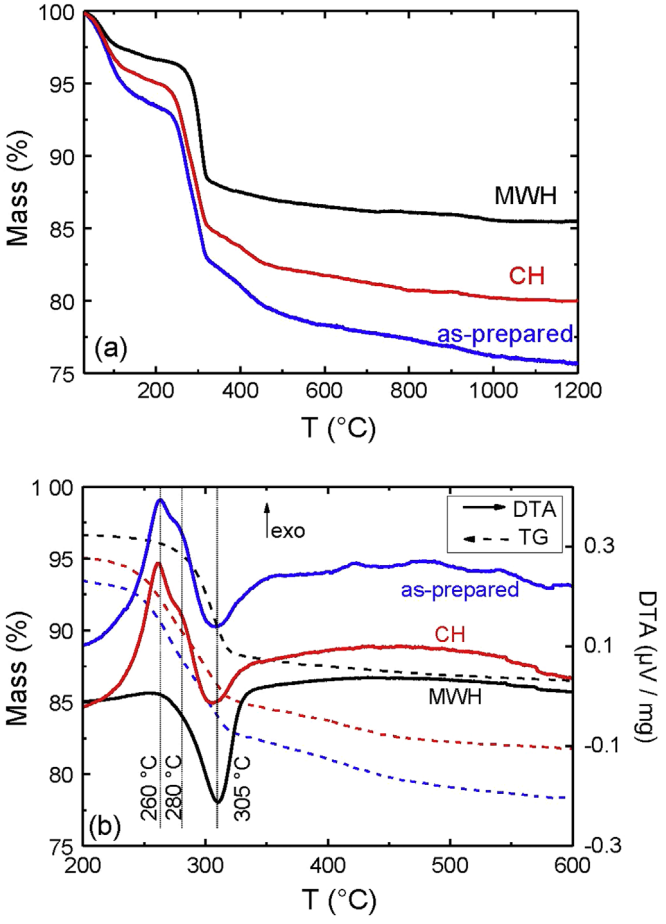

Fig. 1. Thermogravimetric curves (a) and differential thermal analyses (b) of the as-prepared, conventional heating (CH), and microwave-assisted hydrothermal (MWH) treated NiO–YSZ–CeO_2 powders.

associated with at least two convoluted exothermic peaks and one endothermic, as shown in Fig. 1b. The convoluted exothermic peak is attributed to the crystallization of ceria (~260 °C) [27] and nickel hydroxide (~280 °C). Such attributions were confirmed by performing separated thermal analyses of both NiO and CeO_2 co-precipitated precursors (not shown). The exothermic peaks are more pronounced in both the as-prepared and CH samples, whereas for the MWH sample the exothermic events were essentially suppressed. The absence of exothermic peaks indicates the presence of crystalline nickel hydroxide in the MWH powders. The endothermic peak at $T=305$ °C in DTA curve is possibly related to dehydroxylation of nickel hydroxide to nickel oxide [28] ($Ni(OH)_2 \rightarrow NiO + H_2O$), which is likely to be the main event associated with the second mass loss. Such a mass loss (~10%) was similar for all samples, indicating that it is associated with nickel phase. The as-prepared and CH samples showed a third mass loss region (~390 °C) of ~2%, occurring after nickel hydroxide thermal decomposition that is probably due to the removal of chemically adsorbed water and nickel oxide hydration water.

The powders were calcined at 500 °C for 4 h and semi quantitative chemical analyses were carried out by EDX. Table 1 summarizes the phase compositions in oxide phases calculated from EDX results. HfO_2 is an impurity usually present in zirconia powders and was found as a minor phase. The phase compositions were similar for the three samples, with average values being NiO: YSZ:CeO_2=23:69:7 (wt%). Such composition corresponds to ~27 vol% of NiO, which is close to the percolation threshold of the semiconducting phase. However, such values are considerably below the nominal ones due to losses of Ni during the coprecipitation [9,11].

The influence of thermal treatments were on the NiO–YSZ–CeO_2 composites further analyzed by X-ray diffraction (XRD), as shown in the Fig. 2.

The XRD data were indexed by comparison with standard files hexagonal β-$Ni(OH)_2$ (JCPDS 14-117), cubic YSZ (JCPDS 82-1246), cubic CeO_2 (JCPDS 34-394), and cubic NiO (JCPDS 47-1049). All the observed peaks corresponded to the indexed phases and no spurious phases were detected by the XRD. In Fig. 2a, the diffraction peaks of β-$Ni(OH)_2$ are clearly observed in the MWH sample, while for both the as-prepared and CH powders the most intense $Ni(OH)_2$ peak (101) at 2θ~39° is not visible. Such a result adds evidence to the relation between the suppression of the exothermic peak occurring at 280 °C (Fig. 1b) and the presence of crystalline nickel hydroxide in the MWH sample.

After calcining step at 500 °C the β-$Ni(OH)_2$ was converted to NiO and all samples exhibited similar XRD patterns (Fig. 2b). The crystallite sizes of the calcined powders were calculated using the Debye–Scherrer formula and the selected peaks corresponding to the maximum relative intensity of each phase: the (311) reflection at 2θ~59° for NiO, and the (111) reflection at 2θ~30° for YSZ. Such analysis was not possible for CeO_2 since it has a relative small concentration and possibly very small crystallite size, as inferred from the low intensity and broad diffraction peak at 2θ~28° (Fig. 2b). The crystallite sizes, listed in Table 2, are ~9 nm and 20 nm for NiO and YSZ, respectively. Such values are in good agreement with previously reported ones for similar calcining

Table 1
Phase composition (wt%) calculated from EDX analysis.

	As-prepared	CH	MWH
NiO	23.1	23.1	22.4
YSZ	68.9	68.9	69.6
CeO_2	6.8	6.9	6.9
HfO_2	1.2	1.1	1.1

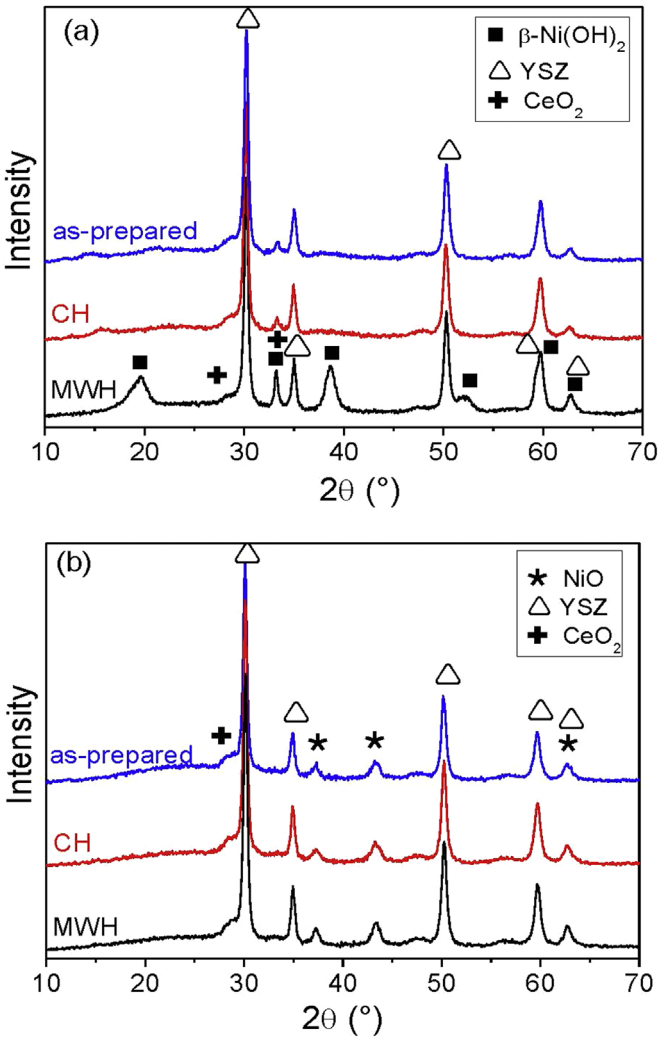

Fig. 2. X-ray diffraction patterns of synthesized (a) and calcined at 500 °C (b) powders of NiO–YSZ–CeO_2.

temperature [29]. It is interesting to note that the MWH samples display the largest crystallite size of NiO, a feature possibly related to the earlier crystallization of the precursor phase β-$Ni(OH)_2$ as compared to the other samples. The lattice parameters (a) were calculated and shown in Table 2. Both YSZ and NiO were found to have lattice parameters in good accordance with values of the corresponding JCPDS files.

Table 2
Crystallite sizes and lattice parameters (a) obtained for calcinated powders, green (ρ_0), apparent densities (ρ), and fraction of the theoretical density (ρ/ρ_T).

		as-prepared	CH	MWH
		Crystallite sizes (nm)		
NiO		8.7	7.7	9.4
YSZ		19.7	20	19.4
		***a* (Å)**		
NiO		4.182(1)	4.181(1)	4.194(1)
YSZ		5.142(1)	5.142(1)	5.143(1)
		Density (g cm^{-3})		
TMA	ρ	5.77	5.67	5.84
(1400 °C)	ρ_0	2.83	–	2.71
IS	ρ	5.04(6)	5.04(5)	5.19(9)
(1200 °C)	ρ/ρ_T **(%)**	82.2(9)	81.8(8)	84.8(9)

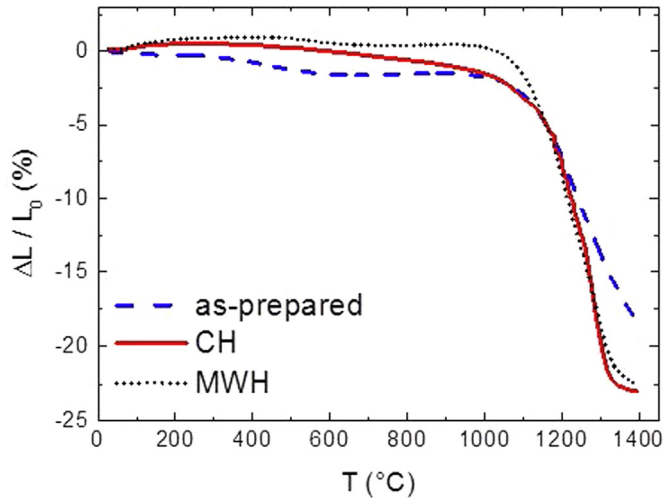

Fig. 3. Linear shrinkage of NiO–YSZ–CeO_2 compacts.

The sintering behavior of ceramic compacts was studied by dilatometry analysis, as shown in Fig. 3. The total retraction observed for compacts prepared with calcined powders were 19%, 22%, and 23% for the as-prepared, CH, and MWH, respectively (Fig. 3a). Such total retractions are in agreement with the green density (ρ_0) values shown in Table 2. From room temperature up to ~1100 °C samples display negligible retraction. Both the onset of the shrinkage (~1050 °C) and the maximum densification rate temperature (~1280 °C) are weakly dependent on the heat treatment. However, at the maximum measuring temperature the as-prepared sample has not attained the final sintering stages, whereas both CH and MWH samples display a flattening of the retraction curve suggesting the end of the sintering process at T~1400 °C. The final apparent densities of samples were similar, but the MWH showed slightly higher values than the other samples (Table 2).

The effect of the different thermal treatments on the properties of the NiO–YSZ–CeO_2 ceramic compacts sintered at 1200 °C was studied. The apparent densities of the samples sintered at 1200 °C (Table 2) are similar, but the MWH sample displayed slightly higher values, in agreement with the dilatometry (Fig. 3). Phase characterization of sintered samples by XRD is shown in Fig. 4. The XRD data of sintered samples exhibit only the peaks corresponding to both the NiO and YSZ. Differently from the calcined samples, the high sintering temperature promoted the formation of the

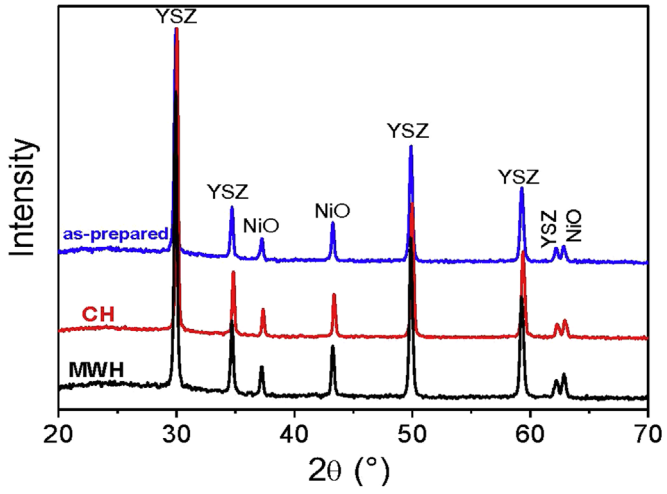

Fig. 4. X-ray diffraction patterns of NiO–YSZ–CeO_2 samples sintered at 1200 °C.

solid solution YSZ:CeO_2 [30]. The calculated lattice parameters (a) for YSZ:CeO_2 phase are $a_{YSZ:Ce}$=5.169(2) Å and 5.173(2) Å for as-prepared and MWH samples, respectively. Cerium has larger ionic radius than zirconium promoting an increase of the lattice parameter [31]. Thus, lattice parameter of sintered samples are higher than the ones calculated for calcined samples (Table 2), because the solid solution between YSZ and CeO_2 at high temperature. By using the Vegard's law [32] and the measured mass fraction of CeO_2 by EDX (corresponding to ~7 mol%) it is possible to calculate the lattice parameter of the cubic solid solution $a_{YSZ:Ce}$=5.168 Å. Such value is excellent agreement to the one calculated by the XRD and indicates that ceria formed a complete solid solution with YSZ. On the other hand, NiO exhibits lattice parameters (a_{NiO}=4.183 Å) similar to those in Table 2.

Fractured surfaces of the ceramics were observed in a FEG-SEM microscope (Fig. 5). Secondary electron images in Fig. 5 display phase contrast, being NiO particles darker than YSZ:CeO_2 ones, as confirmed by EDS analyses (not shown). Low magnification images (Fig. 5a and c) reveal an irregular microstructure with a good dispersion of NiO and a relatively high porosity, which was expected considering the calculated ρ/ρ_T~82% for the compacts sintered at 1200 °C (Table 2). Both samples exhibit similar microstructure composed of denser regions, with larger concentration of brighter YSZ:CeO_2 grains, separated by more porous regions in which NiO particles are predominant (Fig. 5a and c). Higher magnification images (Fig. 5b and d) reveal that grain sizes are in the submicrometric range. NiO particles have a faceted shape, whereas YSZ:CeO_2 exhibit a more rounded form. Nevertheless, it is possible to compare in Fig. 5b and d that average grain size in the as-prepared samples is considerably smaller than that of the MWH sample, a feature more pronounced for the darker NiO grains. A rough estimate of grain size during FEG-SEM analysis indicated typical NiO grain sizes of ~450 nm for the as-prepared sample, while MHW sample have grains with diameter ~750 nm. Such a difference is likely to arise from the microwave heat treatment during powder synthesis and it is in agreement with the formation of crystalline Ni phases at early stages of the synthesis promoted by the MHW, as shown in Figs. 1 and 2. Moreover, the larger grain size of the MWH is in accordance with the higher crystallite size calculated from XRD data (Table 2).

The observed microstructural features are reflected on the electrical properties of the composites. The IS diagrams measured between 300 °C and 700 °C are shown in Fig. 6. For T < 500 °C (Fig. 6a and b), the IS diagrams exhibit a well-defined high frequency semicircle (relaxation frequency f_0 > 100 kHz) and a low frequency component in which at least two components could be discerned: one in the frequency range 100 Hz < f < 10 kHz and another at lower frequencies (f < 100 Hz). However, a direct attribution to each IS component is not straightforward due to the complex microstructure of composite samples that exhibit different charge carriers and a rather complex distributions of both grain size and pores. Thus, analyses of the IS data were focused on the conductivity of the two components that could be more easily separated. For T < 500 °C it was possible to separate the high and low frequency components using a series-connected parallel R-CPE equivalent circuit model [24,25,33]. At higher measuring temperature (> 500 °C), only the total electrical resistance was determined at the intercept of the low frequency data with the real axis. With increasing measuring temperature (Fig. 6c) the high frequency semicircle rapidly decreases and the total resistance is dominated by the low frequency components, as shown in the impedance diagram measured at T ≥ 500 °C (Fig. 6c and d). For both the as-prepared and CH samples the magnitude of the electrical resistance associated with each frequency component were very similar in the whole temperature range. Interestingly, the MWH sample exhibited a different behavior. For T < 500 °C the

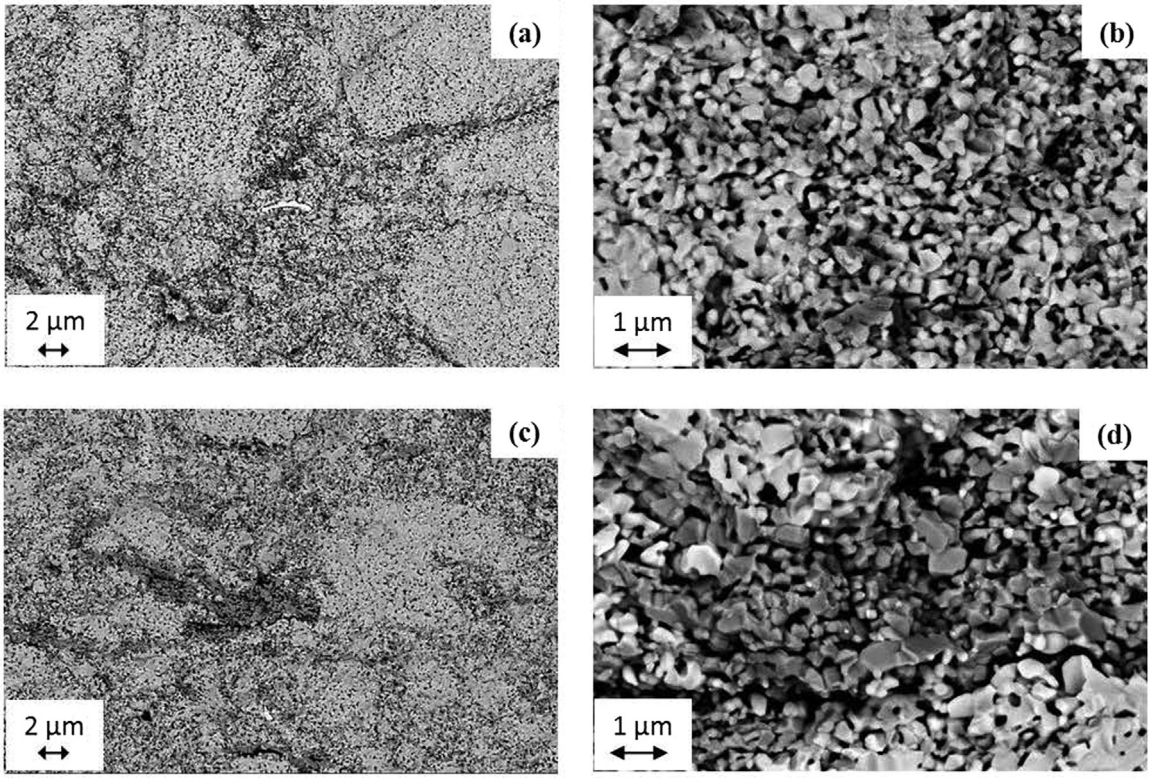

Fig. 5. FEG-SEM images of fractured surfaces of as-prepared (a, b) and MWH (c, d) samples.

MWH showed the highest electrical resistance, being all the frequency components significantly more resistive than the corresponding ones of the other samples. Nevertheless, with increasing measuring temperature, the MWH sample becomes less resistive and at $T \sim 500$ °C (Fig. 6c) all samples have comparable IS diagrams.

Apparently, the low frequency components are responsible for the different electrical behavior of such mixed ionic–electronic composites [32,34]. Therefore, IS diagrams were analyzed to compute the respective Arrhenius plots. Fig. 7 shows the Arrhenius plots of the electrical resistivity of both high (Fig. 7a) and low (Fig. 7b) frequency components at low $T < 500$ °C, and the total resistance (Fig. 7c). Analyzing the Arrhenius plots revealed important features concerning the electrical properties of the composites.

At low temperatures ($T < 500$ °C) the MHW sample has the lowest electrical conductivity, being the low frequency component the main resistive contribution to the total electrical resistivity. At $T < 500$ °C all components exhibited thermally activated transport and the calculated activation energies E_a are displayed on Table 3. Such a difference diminishes with increasing measuring temperature due to the higher E_a of the MWH sample. For $T \geq 500$ °C all samples have comparable electrical conductivity. The high frequency components (Fig. 7a) exhibited calculated E_a (Table 3) that approach the reported values for oxygen ion conduction in YSZ (~ 1 eV). However, the low frequency component (Fig. 7b) has a marked lower E_a for both as-prepared and CH samples (~ 0.75 eV), whereas the MHW sample has similar $E_a \sim 1$ eV irrespectively the frequency range. The observed difference on the activation energy values is a strong evidence that both as-prepared and CH samples have a more mixed ionic–electronic contribution on the low frequency component of the IS diagrams. Such a feature is associated with the contribution of NiO to the electrical transport that decreases the activation energy and increases the conductivity at low temperature [33]. On the other hand, the MHW treatment seems to suppress such a behavior and the low frequency component exhibits considerably higher E_a, compatible with YSZ-based electrolytes. Such an absence of mixed ionic–electronic contribution indicates that electrical properties of the MWH sample is significantly less affected by the electronic conducting phase (NiO), probably due to the different grain size distribution evidenced on Fig. 5.

The Arrhenius plot of the total electrical resistivity (Fig. 7c) reveals that the MHW sample is the only to exhibit a single Arrhenius-like behavior in the entire temperature range, whereas both the as-prepared and CH samples exhibited a deviation from the Arrhenius behavior at $T \sim 450$ °C. The MHW sample showed a linear behavior in the entire temperature range investigated with calculated $E_a \sim 1$ eV, in perfect agreement with the expected behavior of YSZ-based oxygen conductors [1,24,25]. On the other hand, both the as-prepared and the CH samples exhibited two thermally activated processes. For $T < 450$ °C, as-prepared and CH samples have $E_a \sim 0.73$ eV, a value comparable to the ones previously reported for YSZ–NiO mixed ionic–electronic composites [33]. Such relatively low E_a is a strong indication that NiO percolated in the YSZ:CeO_2 matrix at relatively low volume fraction (~ 27 vol%) [5,33]. For $T \geq 500$ °C, all samples exhibited very similar magnitude and temperature dependence of the total electrical conductivity with $E_a \sim 1$ eV. In this T range, the ionic conduction dominates the charge transport and the total electrical conductivity of the MWH sample was slightly higher than the others, possibly due to the higher apparent density.

Differences of the electrical properties revealed by IS data are probably associated with microstructural features resulting from the MWH treatment. The MHW sample exhibits an Arrhenius-like behavior compatible with YSZ-based oxides, while the other samples display a temperature dependence of the electrical conductivity that indicates a mixed-conducting behavior. Similar behavior was previously observed as a function of NiO content [34], i.e., samples with low relative volume fraction of NiO exhibit a

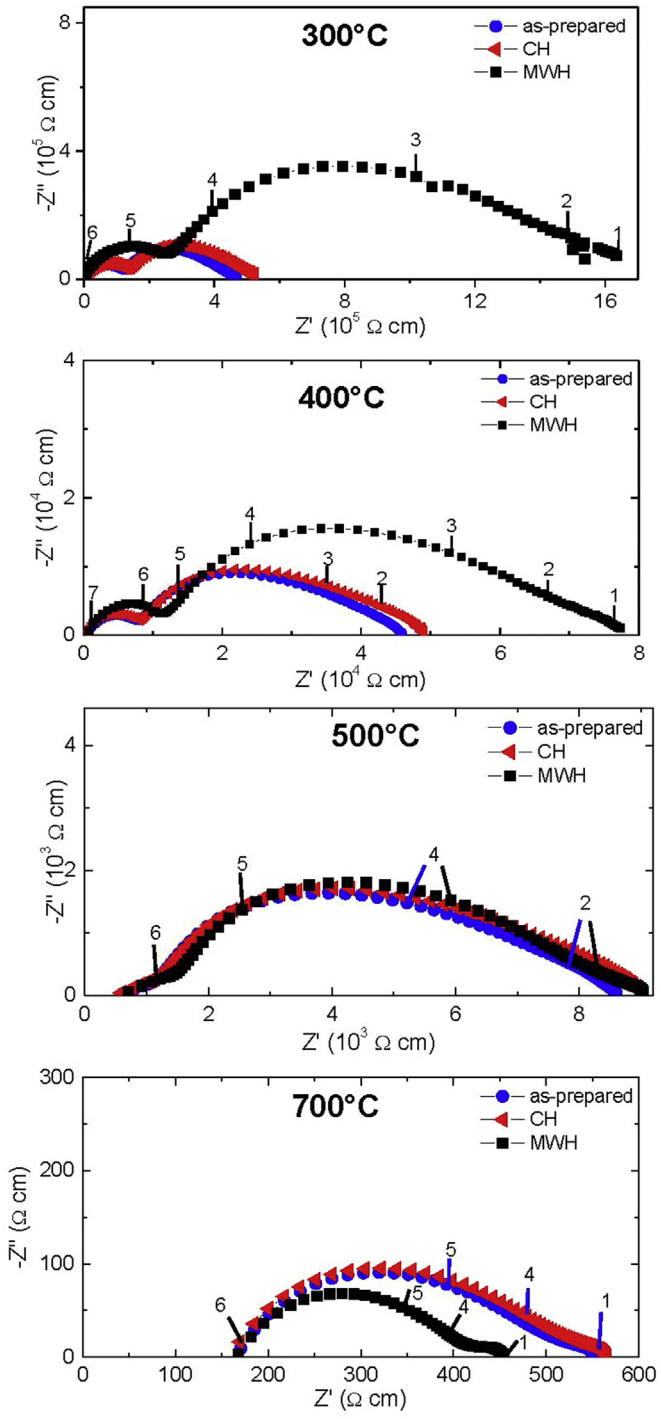

Fig. 6. Impedance diagrams measured at 300 °C, 400 °C, 500 °C, and 700 °C for sintered samples (1200 °C) using the as-prepared, conventional-heated (CH) and microwave-assisted hydrothermal (MWH) powders. Numbers indicate the frequency decimal logarithm.

linear Arrhenius and increasing the volume fraction of NiO results in lower E_a and a deviation of the Arrhenius behavior. The present results indicate that the chemical synthesis method resulted in a good dispersion of phases that allowed the percolation of the NiO. Taking into account that present samples have volume fraction (~27 vol% NiO) close to the percolation threshold of the electronic phase, it is reasonable to expect that minor microstructural changes, such as different average grain size, can disrupt the percolation path of the phases in the composite [5]. The IS and FEG-MEV analyses showed that both as-prepared and CH samples

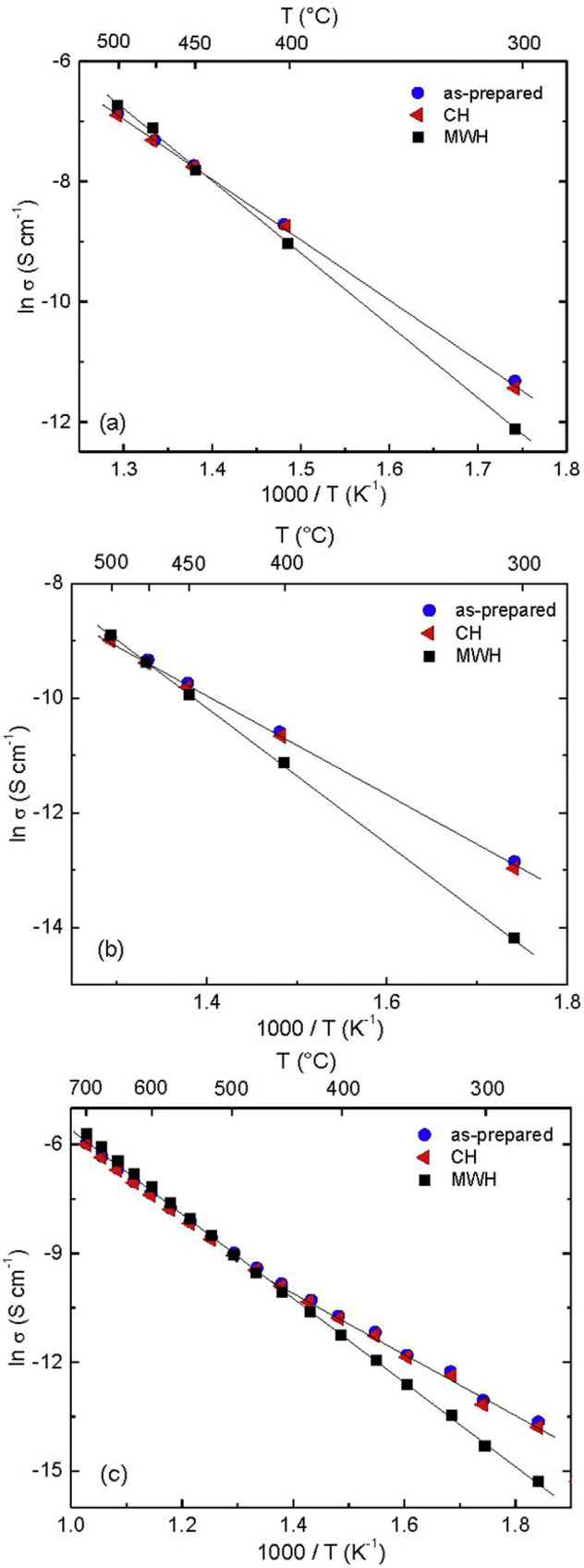

Fig. 7. Arrhenius plots for the high (a), low (b) frequency components and total (c) electrical conductivity. Straight lines correspond to the best linear fitting.

Table 3
Activation energies (E_a) calculated from the Arrhenius plots.

	$T < 500$ °C (Fig. 7a and b)		E_a total (Fig. 7c)	
	High frequency	Low frequency	$T < 500$ °C	$T > 500$ °C
As-prepared	0.85 (5)	0.75(6)	0.73(3)	0.97(1)
CH	0.87(10)	0.76(8)	0.74(2)	0.98(9)
MWH	1.00(13)	1.00(6)	1.03(8)	1.03(9)

have relative average grain size of both phases (YSZ:CeO_2 and NiO) that favor the percolation of the semiconducting phase, a feature more clear at low temperature. On the other hand, the MWH treatment resulted in the crystallization of Ni phases at early stages of the synthesis, which promotes grain growth as compared to the other samples. Such a grain growth in MWH samples, inferred from both XRD and FEG-MEV analyses, decreases the dispersion of NiO in the YSZ:CeO_2 matrix and hinders the percolation path of the phases with marked consequences to the electrical properties of the composite.

4. Conclusion

The effects of a microwave hydrothermal (MWH) treatment during synthesis of NiO–YSZ–CeO_2 composites were investigated and compared to a conventional heat treatment. Thermal analysis and X-ray diffraction indicated that the microwave-assisted hydrothermal treatment favors the formation of crystalline β-nickel hydroxide at low temperature. Such Ni-phase crystallizing at early stages of the ceramic processing is likely to result in larger NiO grain on sintered samples. Therefore, the electrical properties of the composites showed that the microwave-treated sample has an Arrhenius-like behavior characteristic of YSZ-ionic conductors, whereas the remaining samples have a more clear contribution of the semiconducting NiO. Such difference was attributed to the disruption of the percolating path of NiO due to larger grain size promoted by the microwave treatment. The presented results evidence the importance of a detailed control of the processing of mixed ionic–electronic composites.

Acknowledgments

Thanks are due to the partial funding of, CNEN, FAPESP (2013/26961-7, 2014/50279-4, and 2014/09087-4), and CNPq (554576/2010-4). FCF, AEM, and LBP are thankful for CNPq Scholarships FCF (300961/2013-8).

References

[1] N.Q. Minh, Ceramic fuel-cells, J. Am. Ceram. Soc. 76 (1993) 563–588.
[2] P. Serp, M. Corrias, P. Kalck, Carbon nanotubes and nanofibers in catalysis, Appl. Catal. A 253 (2003) 337–358.
[3] B.S. Prakash, S.S. Kumar, S.T. Aruna, Properties and development of Ni/YSZ as an anode material in solid oxide fuel cell: a review, Renew. Sust. Energy Rev. 36 (2014) 149–179.
[4] M.S. Khan, S.-B. Lee, R.-H. Song, J.-W. Lee, T.-H. Lim, S.-J. Park, Fundamental mechanisms involved in the degradation of nickel–yttria stabilized zirconia (Ni–YSZ) anode during solid oxide fuel cells operation: a review, Ceram. Int. 42 (2016) 35–48.
[5] D.S. Mclachlan, M. Blaszkiewicz, R.E. Newnham, Electrical-resistivity of composites, J. Am. Ceram. Soc. 73 (1990) 2187–2203.
[6] V Esposito, D.Z. De Florio, F.C. Fonseca, E.N.S. Muccillo, R. Muccillo, E. Traversa, Electrical properties of YSZ/NiO composites prepared by a liquid mixture technique, J. Eur. Ceram. Soc. 25 (2005) 2637–2641.
[7] M. Marinsek, K. Zupan, J. Macek, Preparation of Ni–YSZ composite materials for solid oxide fuel cell anodes by gel-precipitation method, J. Power Sources 86 (2000) 383–389.
[8] A. Ringuedé, D. Bronine, J.R. Frade, Assessment of Ni/YSZ anodes prepared by combustion synthesis, Solid State Ion. 146 (3–4) (2002) 219–224.
[9] C. Ding, K. Sato, J. Mizusaki, T. Hashida, A comparative study of NiO–$Ce_{0.9}Gd_{0.1}O_{1.95}$ nanocomposite powders synthesized by hydroxide and oxalate coprecipitation methods, Ceram. Int. 38 (2012) 85–92.
[10] M.D. Liang, B. Yu, M.F. Wen, Y.C. Zhai, Preparation of nanosized NiO/YSZ composite powders by situ-precipitation method, Rare Metal. Mater. Eng. 38 (2009) 443–446.
[11] W.K. Yoshito, V. Ussui, D.R.R. Lazar, J.O.A. Paschoal, Synthesis and characterization of NiO–8YSZ powders by coprecipitation route, Mater. Sci. Forum 498–499 (2005) 612–617.
[12] C.M. Grgicak, R.G. Green, W.F. Du, J.B. Giorgi, Synthesis and characterization of NiO–YSZ anode materials: precipitation, calcination, and the effects on sintering, J. Am. Ceram. Soc. 88 (2005) 3081–3087.
[13] G.A. Tompsett, W.C. Conner, K.S. Yngvesson, Microwave synthesis of nanoporous materials, ChemPhysChem 7 (2006) 296–319.
[14] H. Mohebbi, T. Ebadzadeth, F.A. Hesari, Synthesis of nano-crystalline NiO–YSZ by microwave-assisted combustion synthesis, Powder Technol. 188 (2009) 183–186.
[15] K. Tahmasebi, M.H. Paydar, Microwave assisted solution combustion synthesis of alumina-zirconia, ZTA, nanocomposite powder, J. Alloy. Compd. 509 (2011) 1192–1196.
[16] B. Vaidhyanathan, D.K. Agrawal, R. Roy, Novel synthesis of nitride powders by microwave-assisted combustion, J. Mater. Res. 15 (2000) 974–981.
[17] G.J. Choi, H.S. Kim, Y.S. Cho, $BaTiO_3$ particles prepared by microwave-assisted hydrothermal reaction using titanium acylate precursors, Mater. Lett. 41 (1999) 122–127.
[18] K.H. Kim, H.C. Park, S.D. Lee, W.J. Hwa, S.-S. Hong, G.-D. Lee, S.S. Park, Preparation of submicron nickel powders by microwave-assisted hydrothermal method, Mater. Chem. Phys. 92 (2005) 234–239.
[19] Y.B. Khollam, A.J. Deshpande, H.S. Patil, S.B. Deshpande, S.K. Date, Synthesis of yttria stabilized cubic zirconia (YSZ) powders by microwave-hydrothermal route, Mater. Chem. Phys. 71 (2001) 235–241.
[20] E.T. Thostenson, T.-W. Chow, Microwave processing: fundamentals and applications, Compos. Part A 30 (1999) 1055–1071.
[21] J. Feng, J. Qiao, W. Sun, P. Yang, H. Li, Z. Wang, K. Sun, Characteristic and preparation of $Ce_{0.5}Zr_{0.5}O_2$ as the anode support for solid oxide fuel cells by phase inversion technology, Int. J. Hydrog. Energy 40 (2015) 12784–12789.
[22] M.G. Zimicz, D.G. Lamas, S.A. Larrondo, $Ce_{0.9}Zr_{0.1}O_2$ nanocatalyst: influence of synthesis conditions in the reducibility and catalytic activity, Catal. Commun. 15 (2011) 68–73.
[23] A.S. Ferlauto, D.Z. de Florio, F.C. Fonseca, V. Esposito, R. Muccillo, E. Traversa, L. O. Ladeira, Chemical vapor deposition of multi-walled carbon nanotubes from nickle/yttria-stabilized zirconia catalysts, Appl. Phys. A 84 (2006) 271–276.
[24] P. Scherrer, P. Göttinger Nachrichten, Math. Phys. 2 (1918) 98–100.
[25] F.C. Fonseca, R. Muccillo, Impedance spectroscopy of (yttria-stabilized zirconia)-magnesia ceramic composites, Solid State Ion. 131 (2000) 301–309.
[26] F.C. Fonseca, R. Muccillo, Impedance spectroscopy analysis of percolation in (yttria-stabilized zirconia)–yttria ceramic composites, Solid State Ion. 166 (2004) 157–165.
[27] B. Djuricic, S. Pickering, Nanostructured cerium oxide: preparation and properties of weakly-agglomerated powders, J. Eur. Ceram. Soc. 19 (1999) 1925–1934.
[28] T. Subbaiah, R. Mohapatra, S. Mallick, K.G. Misra, P. Singh, R.P. Das, Characterisation of nickel hydroxide precipitated from solutions containing Ni^{2+} complexing agents, Hydrometallurgy 68 (2003) 151–157.
[29] K.W. Schlichting, N.P. Padture, P.G. Klemens, Thermal conductivity of dense and porous yttria-stabilized zirconia, Journal. Mater. Sci. 36 (2001) 3003–3010.
[30] Y. Hinatsu, T. Muromura, Phase relations in the systems ZrO_2–Y_2O_3–Nd_2O_3 and ZrO_2–Y_2O_3–CeO_2, Mater. Res. Bull. 21 (1986) 1343–1349.
[31] R.D. Shannon, Revised effective ionic radii and systematic studies of interatomic distances in halides and chalcogenides, Acta Cryst. A 32 (1976) 751–767.
[32] C. Wang, Y. Wang, W. Huang, B. Zou, Z.S. Khan, Y. Zhao, J. Yang, X. Cao, Influence of CeO_2 addition on crystal growth behavior of CeO_2–Y_2O_3–ZrO_2 solid solution, Ceram. Int. 38 (2012) 2087–2094.
[33] F. Teocoli, D.W. Ni, S. Sanna, K. Thyden, F.C. Fonseca, V. Esposito, Fast mass interdiffusion in ceria/alumina composite, J. Mater. Chem. A 3 (2015) 17135–17143.
[34] F.C. Fonseca, D.Z. De Florio, V. Esposito, E. Traversa, E.N.S. Muccillo, R. Muccillo, Mixed ionic-electronic YSZ/Ni composite for SOFC anodes with high electrical conductivity, J. Electrochem. Soc. 153 (2006) A345–A360.